chemosensors

Article

Photoluminescence Sensing of Chloride Ions in Sea Sand Using Alcohol-Dispersed $CsPbBr_3$@SiO_2 Perovskite Nanocrystal Composites

Henggan Li [1,†], Feiming Li [2,3,†], Yipeng Huang [2], Linchun Zhang [2], Min Ye [2], Jingwen Jin [2] and Xi Chen [2,*]

[1] Department of Civil Engineering and Architecture, Wuyi University, Wuyishan 354300, China; lhg@wuyiu.edu.cn
[2] Department of Chemistry and the MOE Key Laboratory of Spectrochemical Analysis & Instrumentation, College of Chemistry and Chemical Engineering, Xiamen University, Xiamen 361000, China; lfm1914@mnnu.edu.cn (F.L.); huangyp@glut.edu.cn (Y.H.); 20520191151446@stu.xmu.edu.cn (L.Z.); 20520201151887@stu.xmu.edu.cn (M.Y.); 20520191151435@stu.xmu.edu.cn (J.J.)
[3] College of Chemistry, Chemical Engineering and Environment, Minnan Normal University, Zhangzhou 363000, China
* Correspondence: xichen@xmu.edu.cn; Tel.: +86-592-2184530
† These authors contributed equally to this work.

Abstract: In this study, $CsPbBr_3$@SiO_2 perovskite nanocrystal composites ($CsPbBr_3$@SiO_2 PNCCs) were synthesized by a benzyl bromide nucleophilic substitution strategy. Homogeneous halide exchange between $CsPbBr_3$@SiO_2 PNCCs and Cl^- solution (aqueous phase) was applied to the determination of Cl^- in sea sand samples. Fast halide exchange with Cl^- in the aqueous phase without any magnetic stirring or pH regulation resulted in the blue shift of the photoluminescence (PL) wavelength and vivid PL color changes from green to blue. The results show that the PL sensing of Cl^- in aqueous samples could be implemented by using the halide exchange of $CsPbBr_3$@SiO_2 PNCCs. A linear relationship between the PL wavelength shift and the Cl^- concentration in the range of 0 to 3.0% was found, which was applied to the determination of Cl^- concentration in sea sand samples. This method greatly simplifies the detection process and provides a new idea for further broadening PL sensing using the $CsPbBr_3$ PNC halide.

Keywords: $CsPbBr_3$ perovskite nanocrystal composites; colorimetric sensing; photoluminescence wavelength shift; sea sand; Cl^-

check for updates

Citation: Li, H.; Li, F.; Huang, Y.; Zhang, L.; Ye, M.; Jin, J.; Chen, X. Photoluminescence Sensing of Chloride Ions in Sea Sand Using Alcohol-Dispersed $CsPbBr_3$@SiO_2 Perovskite Nanocrystal Composites. *Chemosensors* **2022**, *10*, 170. https://doi.org/10.3390/chemosensors10050170

Academic Editors: Jin-Ming Lin and Qiongzheng Hu

Received: 11 April 2022
Accepted: 29 April 2022
Published: 2 May 2022

Publisher's Note: MDPI stays neutral with regard to jurisdictional claims in published maps and institutional affiliations.

Copyright: © 2022 by the authors. Licensee MDPI, Basel, Switzerland. This article is an open access article distributed under the terms and conditions of the Creative Commons Attribution (CC BY) license (https://creativecommons.org/licenses/by/4.0/).

1. Introduction

Due to environmental protection, the mining of river sand is restricted, which results in the shortage of river sand resources for buildings. The replacement of sea sand necessitates the use of river sand. However, sea sand without suitable treatment causes serious problems for the durability of reinforced concrete structures due to the high concentration of chloride ions (Cl^-). The durability of concrete in coastal or offshore areas is mainly caused by Cl^- erosion, which may be widespread in a relatively large area. The occurrence of chlorinated sand is generally associated with two situations: one is that chlorinated sea sand is inadequately cleaned and is then used in the mixing of concrete, and the second is that some rivers are polluted by seawater due to seawater backflow. In this case, a certain amount of river sand exceeding the standard of Cl^- enters the commercial market. Research results show that the possibility and harm of reinforcement corrosion increase with the increase in Cl^- content in concrete. When the concentration of Cl^- exceeds the critical concentration (generally considered to be 0.6 kg/m^3), corrosion occurs in the presence of water and oxygen.

The titration of a potassium chromate indicator with silver nitrate has been commonly regarded as a typical titration method for the determination of Cl^- according to the Chinese

National Standard (GB/T 14684-2011) for construction sand [1]. When potassium chromate reacts with silver nitrate, silver chromate appears with a brick-red color, but the color changes to white as soon as Cl^- is added. There have been many instrumental methods for the determination of Cl^- in aqueous samples, such as high-performance liquid chromatography [2], ion chromatography [3], capillary electrophoresis [4], the electrochemical method [5], the fluorescence method [6] and the colorimetric detection method [7]. However, sophisticated scientific instruments with complicated data-collecting and -processing systems are required, and thus, high costs and the requirement for a professional operator severely limit their usage.

Although selective electrodes can be applied for the inexpensive and convenient sensing of Cl^- in some samples, such as human serum [8,9], the response sensitivity and long-term stability of the electrochemical sensing material should be thoroughly considered. Based on the situation, fluorescence-sensing methods can be reasonably considered. At present, fluorescence-sensing methods for Cl^- mainly include fluorescence on and quenching approaches. In 2020, Zhang et al. [10] synthesized 5, 10, 15, 20-tetra (4-hydroxyphenyl) porphyrin (THPP) and coordinated it with Ag^+ to form a THPP-Ag complex. This complex has a strong binding ability to Cl^- and can be used for Cl^- fluorescence sensing with a detection limit of 7.5 μM Cl^-. This sensing approach has been successfully applied to in vitro and in vivo bioimaging. Based on the strong interaction between silver (Ag^+) and Cl^-, a Ag^+-benzimidazole complex (Ag^+-FBI) was used by Kim et al. [6] to develop a fluorescence sensor for the quantitative determination of Cl^- in human sweat. The fluorescence intensity of the Ag^+-FBI complex increased in the presence of Cl^-, with a detection limit of 19 μM and a response time of less than 3 min. The Ag^+-FBI complex showed high selectivity for Cl^- ions in a wide pH range from pH 6 to pH 9. In 2021, Tutol et al. [11] reported a fluorescence on-type sensing approach for the determination of Cl^- in detergent and *E. coli* using a single point mutation of the fluorescent protein. The single point mutation replaces the chromophore counter-ion with valine, creating a binding site for Cl^-. The binding of Cl^- adjusts the pKa of chromophores to a protonated fluorescence state and responds to the pH change.

In addition, several fluorescence-quenching-based Cl^- sensing approaches have been reported in recent years. For example, in 2006, Schazmann et al. [12] developed a 1, 3-alternating tetra-substituted calix arene-based neutral 2-chloride compound, whose fluorescence could be quenched due to the conformational change during Cl^- coordination. It is highly selective for Cl^- sensing, with a detection limit of 8×10^{-6} M, and the response time is less than 3 s. In 2014, a fluorescence-sensing approach based on the substitution of N-acylhydrazone for Bodipy–mercury (II) was proposed by Madhu et al. [13]. BODIPYs 1 and 2 specifically recognize Hg^{2+} and form 1-Hg^{2+} and 2-Hg^{2+} complexes, respectively, and lead to fluorescence quenching. After Cl^- ions were added to the complexes, fluorescence was restored by extracting mercury (II) ions from the complexes, which reveals high selectivity and specificity under physiological conditions, with a detection limit of 108 nM. In 2015, Bazany-Rodriguez et al. [14] reported a fluorescent dicationic compound for Cl^- sensing in water. Chloride quenches blue fluorescence and forms a very stable complex. This approach revealed good selectivity for other co-existing anions, with a detection limit of 33 mol L^{-1}. In 2017, Kim et al. [15] proposed a fluorescence-quenching sensing approach using citrate-based material, which realized the low-cost and automatic detection of Cl^- in sweat. In addition, the fluorescent material also has higher selective characteristics and can be applied under different pH conditions.

In PL intensity-ratio-based optical sensing, in 2010, Riedinger et al. [16] developed a novel approach for Cl^- sensing using an organic fluorophore (chlorine-sensitive fluorophore, amino-MQAE) and a reference fluorophore (cresol violet)–gold nanoparticle hybrid. The fluorescence quenching of amino-MQAE in the presence of Cl^- can be observed by changing the distance between amino-MQAE and Au NP surfaces with polyethylene glycol (PEG) spacers. In 2020, Ding et al. [17] reported a nanosensor for Cl^- based on the ratio of PL lifetimes. In their study, the luminescent ruthenium dye [Ru(1,10-phenanthroline)$_3$]

was added to the interior of silica nanoparticles, and the external surface was labeled with a fluorescent dye (N,N′-bis-(carboxypropyl)-9,9′-biacridine), which is sensitive towards Cl^-. The surface was further functionalized with a positively charged amino group, and a good linear relationship between the response and Cl^- concentrations from 0 to 200 mM was realized, with the ratio signal varying from 140.9 to 40.2. The proposed method can be used to detect the chloride concentration in cells.

Lead halide perovskites (LHPs) have become smart materials because of their excellent characteristics in photovoltaic and photoelectric fields. For example, in solar cells, the energy conversion efficiency has soared from 3% to 27% in the last 20 years. Recently, lead halide perovskite nanocrystals (LHP NCs) have received great attention for their outstanding photoluminescence (PL) performance, wide color gamut [18], adjustable emission wavelength [19], large defect tolerance [20], high fluorescence quantum yield [21] and unique electrical properties of bipolar transport [22]. These advantages enable LHP NCs to be used in light-emitting diodes, low-threshold lasers, X-ray scintillators and single-photon emitters. Generally, in AMX_3-type LHPs, the A-position is an amine cation such as methylamine, formamidine or Cs^+, the B-position is Pb^{2+}, and the X bit is Cl^-, Br^- or I^- [23]. The energy level structure of LHPs is a key factor affecting its photoelectric performance, which is mainly composed of B and X sites [24]. The valence band of LHPs is hybridized by the NP orbital of the halogen and the 6 s orbital of Pb, while the conduction band is mainly determined by the 6p orbital of Pb, where the np orbital of the halogen contributes less. Thus, by changing halogens with different np orbital energy levels (Cl^- 3*p*, Br^- 4*p* and I^- 5*p*), the band gap of LHPs can be easily adjusted to convert the halogens from chlorine atoms to iodine atoms, and the light emitted by the resulting LHPs can be converted from near-ultraviolet to near-infrared light. Introducing different proportions of halide species to occupy the X position can flexibly adjust the band gap of the resulting LHPs, thus continuously adjusting the emission spectrum to extend to the entire visible range [25]. For example, $CsPbCl_3$ NCs with a particle size of 12 nm produce blue light emission (~450 nm), $CsPbBr_3$ NCs with a particle size of 20 nm emit green light (~520 nm), and $CsPbI_3$ NCs with a particle size of 40–50 nm yield red light (~690 nm). In contrast, the cations at the A position do not play a significant role in the emission wavelength shift of LHPs; for example, the substituent MA^+ can achieve a smaller red shift in the emission spectrum of $CsPbBr_3$ [26].

Recently, there have been several reports on the studies and applications of colorimetric sensing based on the wavelength shift of the halogen exchange characteristics of $CsPbX_3$ NCs. Different halide ions resulted in the variational emission characteristics of the test paper, and 8 μM of fluorine ions, 75 μM of chloride ions and 2 μM of iodide ions in water could be detected. $CsPbX_3$ NCs in transparent nanoporous glass (NPG) were obtained by Ye et al. [27] using a solution immersion method. The prepared material revealed a stimulus-sensing response by changing color in deionized water and non-aqueous solution containing Br^-. They found that the residual Cl^- in NPG nanopores during the preparation of blank NPG played an important role in the sensing response behavior and long-term water resistance. The residual Cl^- ions are responsible for the stimulus conversion of the composite material color from green or red to blue. Even when immersed in water for several months, the composite glass still yielded blue emission due to the protection of Cl^-, and the emission could be restored in non-aqueous solution to a green color after treatment with Br^-. Sandeep et al. developed paper-substrate-immobilized $CsPbBr_3$ NCs and used the paper substrate to detect fluorine ions, chloride ions and iodide ions in water [28]. Three approaches for the determination of Cl^- using $CsPbBr_3$ NCs were proposed by Mishra et al. [29], including the direct addition of the Cl^- sample solution to $CsPbBr_3$ NCs, a drop of the Cl^- sample solution onto a glass substrate with deposited $CsPbBr_3$ NCs, and a drop of $CsPbBr_3$ NCs onto a strip pre-soaked in the Cl^- sample solution. In these procedures, the blue shift of their fluorescence spectra could be observed due to the rapid anion exchange between $CsPbBr_3$ NCs and Cl^-, and the detection limit was 100 μM. More recently, Chen et al. [30] investigated the heterogeneous halide exchange between $CsPbBr_3$

PNCs (*n*-hexane, organic phase) and NaCl solutions (aqueous phase). The results show that $CsPbBr_3$ PNCs could achieve fast halide exchanges with Cl^- of NaCl in the aqueous phase, accompanying a significant wavelength blue shift and vivid fluorescence color changes. The Cl^- concentration in sweet samples could be determined with a detection limit of 3 mmol/L.

In this study, we developed an efficient synthesis approach to fabricate $CsPbBr_3@SiO_2$ perovskite nanocrystal composites ($CsPbBr_3@SiO_2$ PNCCs) in 10 min with the help of a nucleophilic substitution strategy using benzylic bromide. Compared with $CsPbBr_3$ PNCs, $CsPbBr_3@SiO_2$ PNCCs revealed better stability towards the alcohol polarity and can stably disperse in ethanol. In addition, the homogeneous halogen exchange process of NaCl solution (water)–$CsPbBr_3@SiO_2$ PNCCs (ethanol) was observed and investigated in the study. In sensing experiments, it was found that the halogen exchange between Cl^- and $CsPbBr_3@SiO_2$ PNCCs could be realized without any pH modifications to the sensing medium or magnetic stirring, which is conducive to the efficient determination of Cl^- and reveals its simplicity and convenience compared with heterogeneous halogen exchange between Cl^- and $CsPbBr_3$ NCs in water–organic phases [30]. The detection limit of 0.05 mg/mL for this approach meets the requirement that the Cl^- content in the highest class of construction sand should generally be lower than 0.1 mg/g. This approach was applied to the fluorescence sensing of Cl^- in sea sand samples.

2. Materials and Methods

2.1. Materials and Chemicals

Octadecene (ODE, 90%), lead stearate (PbSTR, 99.9%), Cs_2CO_3 (99.9%) and 3-aminopropyl triethoxysilane (APTES, 98%) were purchased from Shanghai Aladdin Reagent Co., Ltd., Shanghai, China. ODE was dried for 1 h in a vacuum at 120 °C for purification. 1,3,5-Tris (bromomethyl) benzene (TBB) was obtained from Shanghai Anergy Reagent Co., Ltd., Shanghai, China. Other chemicals were used directly without further purification.

A standard Cl^- solution with a concentration of l000 μg/mL was purchased from Beijing Zhongke Quality Inspection Biotechnology Co. Ltd., Beijing, China. Each different concentration of Cl^- solution was prepared by diluting the standard solution with pure water and used on the same day.

2.2. Instruments

The diffuse reflectance spectra of $CsPbBr_3@SiO_2$ PNCCs were characterized by a near-infrared/UV/visible spectrophotometer (Varian Cary 5000, Cary, NC, USA). Fluorescence spectra were collected by an F-7100 fluorescence spectrophotometer (Hitachi, Tokyo, Japan). An excitation wavelength of 365 nm was used. A 1.5 nm slit for excitation and a 5.5 nm slit for emission were selected. An excitation wavelength of 365 nm was selected, and a typical excitation spectrum at 1.92% (330 mmol/L) Cl^- is shown in Figure S1. The absolute fluorescence quantum yields (PLQYs) were measured using an FS5 fluorescence spectrophotometer (Edinburgh, UK) loaded with a 150 W xenon lamp with a light source of 106 cps. In the PLQY measurement, the excitation slit was set at 0.8 nm, and the emission slit was 0.5 nm. The fluorescence quantum yields were measured and calculated by integrating sphere. The fluorescence lifetimes were characterized by an FLS 980 spectrometer using a 397 nm laser (Edinburgh, UK) and 1 cm quartz cuvette. The crystal structures of products were characterized by Ultima IV X-ray Diffractometer (Rigaku, Tokyo, Japan) with an operating voltage of 40 kV and a current of 15 mA. Infrared spectra of $CsPbBr_3@SiO_2$ PNCCs were collected by a Nicolet IS5 Fourier Transform Infrared Spectrometer (Symerfeld, New York, USA). The surface chemical composition of $CsPbBr_3@SiO_2$ PNCCs was characterized by X-ray photoelectron spectroscopy (XPS, PHI Quantum 2000 Scanning ESCA Microprobe). Tecnai F30 transmission electron microscopy (TEM), high-resolution transmission electron microscopy (HRTEM), and energy-dispersive X-ray spectroscopy (EDX, Philipps-FEI, Netherlands, with an acceleration voltage of 300 kV) were used to analyze the morphology of $CsPbBr_3@SiO_2$ PNCCs.

2.3. Preparation of $CsPbBr_3$@SiO_2 PNCCs

To a 25 mL three-neck flask, 5 mL of ODE, 210 μL of APTES, 0.016 g of Cs_2CO_3, 0.0387 g of PbSTR and 0.071 g of TBB were successively added, stirred vigorously at 2500 rpm and heated rapidly to 120 °C in natural air. The product was cooled using ice water. The primary product with yellow-green color was washed using a mixed solvent of ethyl acetate and n-hexane ($V_{ethyl\ acetate}/V_{n\text{-}hexane}$ = 3:1) and was then centrifuged at 10,000 rpm for 10 min. The product of $CsPbBr_3$@SiO_2 PNCCs at the bottom was collected and dried in vacuum at 60 °C for use.

2.4. Sensing and Sample Preparation

Samples of 15 mg of $CsPbBr_3$@SiO_2 PNCCs were accurately weighed and added to 30 mL of anhydrous ethanol for ultrasonic dispersion. A 1 mL sample of the above-mentioned $CsPbBr_3$@SiO_2 PNCC ethanol solution was taken; 5 μL of NaCl solution with different concentrations (17.55–29.83 mg/g) was added and reacted for 15 min, and 365 nm was used as excitation light. Fluorescence spectra of $CsPbBr_3$@SiO_2 PNCCs before and after halogen exchange were collected by F-7100 fluorometer, and the fluorescence discoloration was observed under a 365 nm UV lamp.

About 500 g of each sand sample was obtained from a sea beach or construction site. Before being weighed, the sand samples were dried at 105 °C for 60 min. Then, 10.00 g of the dried sand sample was weighed and then put into a 25 mL flask with 10 mL of deionized water. The filtrate was collected and stored after ultrasonic extraction for 30 min. For the measurement, 10 μL of sample filtrate was directly added to $CsPbBr_3$@SiO_2 PNCC ethanol solution without prior treatment. The other measurement steps were the same as above.

3. Results and Discussion

3.1. Synthesis of $CsPbBr_3$@SiO_2 PNCCs Based on TBB Nucleophilic Substitution

The synthesis of $CsPbBr_3$@SiO_2 PNCCs was set up as shown in Figure 1. TBB first underwent a nucleophilic substitution reaction with APTES under heating conditions, and the generated HBr reacted with the acid-binding agent Cs_2CO_3, producing CsBr, CO_2 and H_2O. In the meantime, it reacted with PbSTR to yield $PbBr_2$. $CsPbBr_3$ PNCs could be produced by the reaction between CsBr and $PbBr_2$, while APTES reacted with H_2O to generate SiO_2 under the catalysis of HBr, by which the one-step synthesis of $CsPbBr_3$@SiO_2 PNCCs could be realized. As shown by the structural formula in Figure 1b, the imine bond generated by the reaction of TBB with APTES and the products of the unreacted NH_2 with HBr, as well as the unreacted NH_2 of APTES, can be taken as the anchor sites of $CsPbBr_3$ PNCs on the surface of SiO_2 [31,32]. The anchor sites play a key role in the passivation of the $CsPbBr_3$ PNC surface and in improving its stability.

For the synthesis of $CsPbBr_3$ PNCs coated by SiO_2, the whole synthesis process can be carried out in an open system at 120 °C and completed within 10 min. By simply mixing the solvent, all of the precursors and the ligand reagents, strong luminescent $CsPbBr_3$ PNCs@SiO_2 PNCCs can be obtained. In addition, the released amount of H_2O in the synthesis can be regulated by Cs_2CO_3. Compared with the previous method of diffusion hydrolysis of H_2O in the air, the method is more efficient and controllable, which helps to improve the quality of the $CsPbBr_3$@SiO_2 PNCCs for sensing applications.

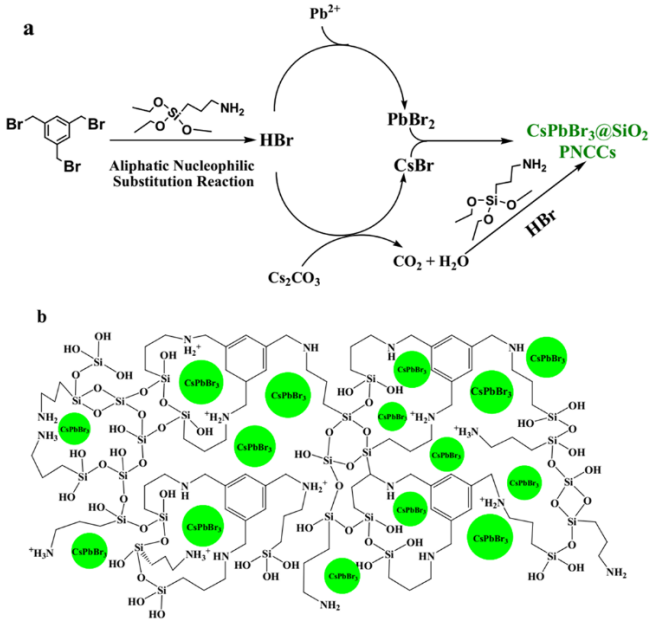


Figure 1. TBB aliphatic nucleophilic substitution-guided synthesis of $CsPbBr_3@SiO_2$ PNCCs (**a**) and corresponding potential structure (**b**).

3.2. $CsPbBr_3@SiO_2$ PNCC Structure and Their Luminescent Characteristics

The structure of the obtained $CsPbBr_3@SiO_2$ PNCCs was characterized by XRD. As shown in Figure 2a, the peaks of 2θ at 15°, 21°, 29°, 33°, 37° and 43° correspond to the crystal planes of {100}, {110}, {200}, {210}, {211} and {220} for cubic crystal $CsPbBr_3$ (cf. PDF#18-0364), indicating the cubic structure of the perovskite crystal in $CsPbBr_3@SiO_2$ PNCCs. No obvious characteristic peak of SiO_2 is observed in the XRD spectrum due to its amorphous structure. FT-IR results, as shown in Figure 2b, show that obvious Si-O stretching vibration peaks are found at 781 cm^{-1}, 902 cm^{-1} and 1117 cm^{-1}. The peak at 3425 cm^{-1} is -OH on SiO_2, indicating the formation of SiO_2. The peak at 1388 cm^{-1} corresponds to the C-N stretching vibration of benzylamine generated after the reaction between TBB and APTES, while the 1468 cm^{-1} peak corresponds to the C-H stretching vibration of the benzene ring of TBB in $CsPbBr_3@SiO_2$ PNCCs, indicating that $CsPbBr_3@SiO_2$ PNCCs have a crosslinked structure. The surface structure of $CsPbBr_3@SiO_2$ PNCCs was further analyzed by XPS, and the peaks at 724.5 and 739.1 eV are attributed to Cs 3D5/2 and Cs 3D3/2. The peaks at 139.0 and 143.6 eV are attributed to the peak at 168.7 eV of Pb 4F7/2 and Pb 4F5/2, the peak at 102.6 eV is attributed to Si 2P, and the peak at 531.3 eV is attributed to O 1s [33]. In addition, the high-resolution XPS spectra of N1s were analyzed, and the peaks at 398.6 eV, 399.8 eV and 401.6 eV are attributed to imine N, amino N and protonated N, respectively. The imine N in the main C-N-C style is from the reaction between TBB and APTES, and the amino N is mainly transferred from NH_2 bonded with TBB. Protonation of N can mainly be obtained from the protonation of the generated imine N and amino N reacting with HBr [32]. Abundant N groups on the surface contribute to the interface passivation of $CsPbBr_3$ PNCs to improve their luminescence performance. In addition, the N groups can also provide anchoring sites for $CsPbBr_3$ PNCs to enhance their stability [32].

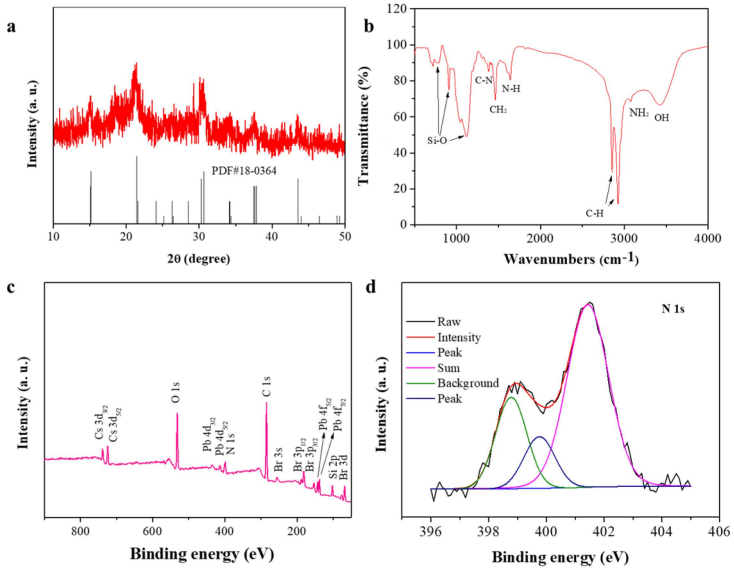


Figure 2. (**a**,**b**) XRD pattern and FT-IR spectra of $CsPbBr_3$@SiO_2 PNCCs; (**c**,**d**) XPS spectra of $CsPbBr_3$@SiO_2 PNCCs and corresponding high−resolution N1s peak.

The structure and composition of $CsPbBr_3$@SiO_2 PNCCs were further characterized by TEM, HRTEM and EDX. As shown in Figure 3, the TEM image of $CsPbBr_3$@SiO_2 PNCCs shows uniform $CsPbBr_3$ PNCs embedded in SiO_2 since the surface of SiO_2 contains many N groups that act as anchor sites for the nucleation and growth of $CsPbBr_3$ PNCs. The larger size distribution of $CsPbBr_3$ PNCs is mainly caused by different microenvironments, as shown in Figure 3a. The content of each element in $CsPbBr_3$@SiO_2 PNCCs, as listed in Figure 3b, was found to be Cs 12.381%, Pb 5.840%, Br 23.050%, Si 18.613% and O 40.114% using EDX.

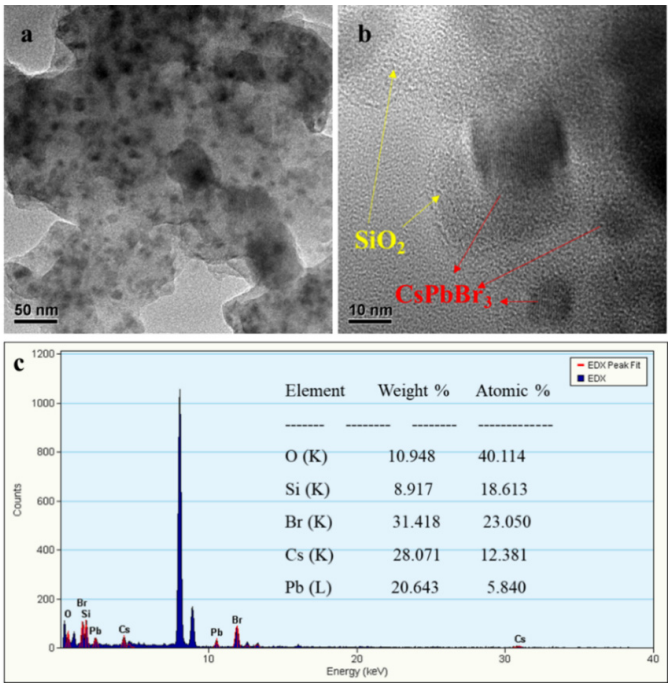


Figure 3. Morphology and chemical composition of $CsPbBr_3$@SiO_2 PNCCs. (**a**) TEM images of $CsPbBr_3$@SiO_2 PNCCs; (**b**) HRTEM image of $CsPbBr_3$@SiO_2 PNCCs. (**c**) EDX analysis of $CsPbBr_3$@SiO_2 PNCCs.

The high-angle annular dark-field imaging of $CsPbBr_3@SiO_2$ PNCCs and the imaging of their element distributions, as shown in Figure 4, indicate that $CsPbBr_3$ PNCs are uniformly distributed in the $CsPbBr_3@SiO_2$ PNCC framework. Cs, Pb, Br, Si and O elements are uniformly distributed in the same contour region, and Pb, Br and Si elements are consistent in the darker position, which is consistent with the TEM results in Figure 3.

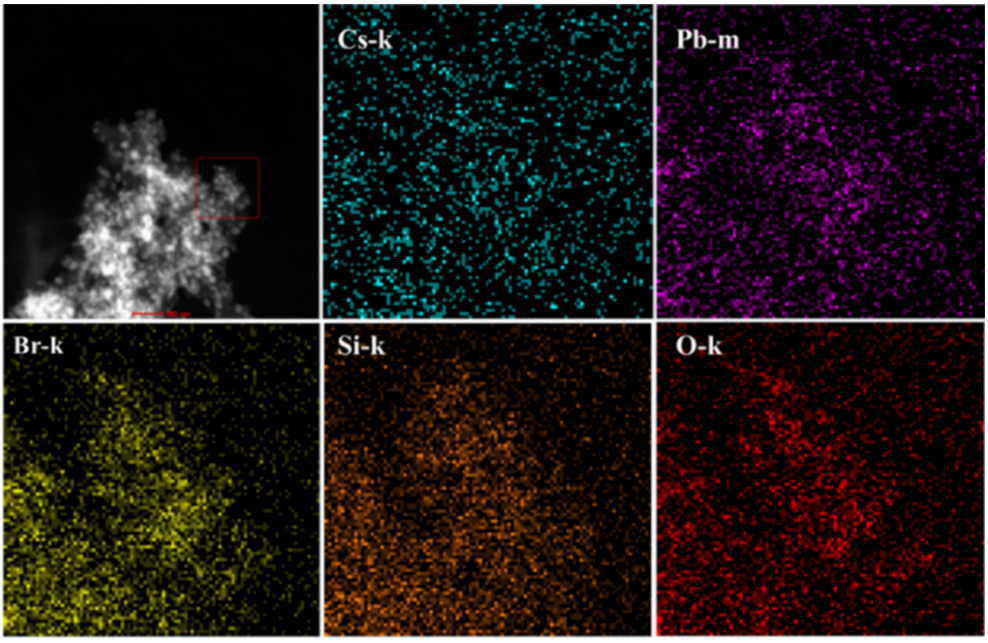


Figure 4. Elemental mapping of Cs, Pb, Br, Si and O of $CsPbBr_3@SiO_2$ PNCCs by TEM.

As shown in Figure 5a, $CsPbBr_3@SiO_2$ PNCCs revealed an emission peak of 513 nm and half-peak width of 22 nm. The fluorescence quantum yield was found to be about 60%. The time-resolved fluorescence attenuation curve of $CsPbBr_3@SiO_2$ PNCCs was fitted with three exponents (Figure 5b), where $\tau = (A_1\tau_1^2 + A_2\tau_2^2 + A_3\tau_3^2)/(A_1\tau_1 + A_2\tau_2 + A_3\tau_3)$, τ_1 is 6.47 ns (A_1 is 33.13%), τ_2 is 23.25 ns (A_2 is 45.03%), τ_3 is 83.52 ns (A_3 is 21.85%), and the total lifetime is about 30.86 ns. The main type of the radiative transition for $CsPbBr_3@SiO_2$ PNCCs results in their excellent luminescence performance due to the good passivation effect of abundant N groups on their surfaces, which inhibits non-radiative transition [34].

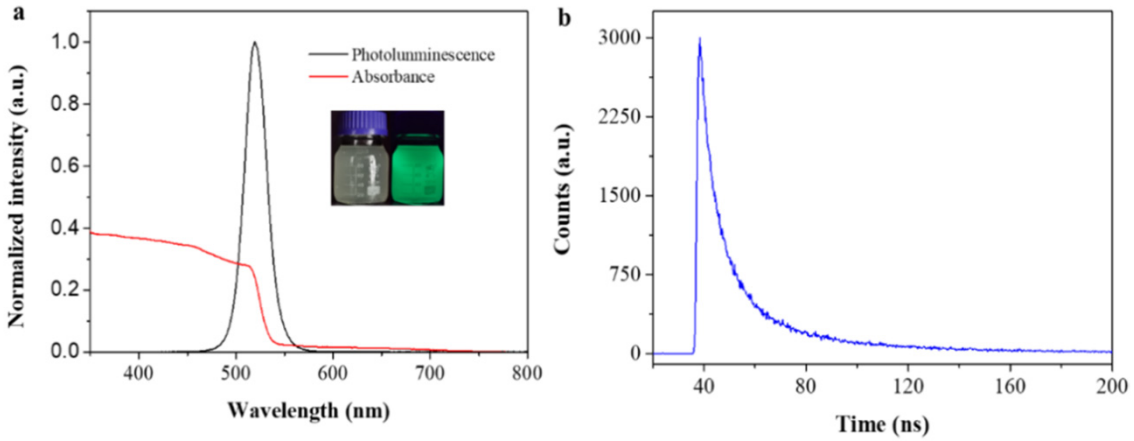


Figure 5. (**a**) Absorption (red line) and PL (black line) spectra of $CsPbBr_3@SiO_2$ PNCCs with a PL maximum at 513 nm, FWHM of 22 nm and PLQY of 60% (inset photograph of $CsPbBr_3@SiO_2$ PNCCs in ethanol solution under (**left**) normal white light and (**right**) a UV lamp with λ of 365 nm); (**b**) time-resolved photoluminescence decay of $CsPbBr_3@SiO_2$ PNCCs.

3.3. Optimization of the Sensing of Cl^-

Generally, $CsPbBr_3$ PNCs are extremely unstable in a polar solution. As indicated in Figure 6a, in ethanol solution, the fluorescence of $CsPbBr_3$ PNCs was attenuated to 30% of its original value in 20 min, and the fluorescence totally disappeared in 60 min due to structural collapse. However, compared with $CsPbBr_3$ PNCs without the SiO_2 coating, $CsPbBr_3$@SiO_2 PNCCs revealed good stability towards ethanol since the SiO_2 coating and the anchoring protection of abundant N groups on the SiO_2 surface will increase the stability of $CsPbBr_3$@SiO_2 PNCCs in a polar solvent. As shown in Figure 6a, $CsPbBr_3$@SiO_2 PNCCs remained at 92% of their original value after their immersion in ethanol for 180 min, which may provide an approach for the homogeneous halogen exchange of $CsPbBr_3$@SiO_2 PNCCs in polar solvents. Subsequently, the effect of H_2O on the stability of $CsPbBr_3$@SiO_2 PNCCs was studied. The results in Figure 6b indicate obvious damage by H_2O to the structure of $CsPbBr_3$@SiO_2 PNCCs, which is different from that in ethanol due to the different solubilities of CsBr (the solubility (25 °C) of CsBr in water and in ethanol is 122.6 g/100 g and 0.3900 g/100 g, respectively [35]). In order to meet the application requirements for the determination of Cl^- in water solution, a suitable volume ratio of ethanol/H_2O of 200/1 (*v*/*v*, typically in experiments, 1 mL ethanol/5 μL H_2O) was selected for further study. In addition, the homogeneous halogen exchange between $CsPbBr_3$@SiO_2 PNCC ethanol solution and NaCl aqueous solution was studied. In contrast to the heterogeneous exchange between $CsPbBr_3$ PNCs *n*-hexane solution and NaCl aqueous solution [30], no pH adjustment or magnetic stirring is needed for the homogeneous halogen exchange. The complete halogen exchange can be realized in 15 min by adding 5 μL of NaCl solution (12.3 mg/g) to 1 mL of $CsPbBr_3$@SiO_2 PNCC ethanol solution, as indicated in Figure 6d. The blue shift of the fluorescence spectrum can be observed in the results shown in Figure 6, and the observed color changes from green to blue. It should be noted that the width of the emission peak broadens after the halogen exchange due to the wide size distribution of $CsPbBr_3$ PNCs in $CsPbBr_3$@SiO_2 PNCCs, as revealed in Figure 3b. Furthermore, the increase in defects on their surfaces leads to a wider emission peak of $CsPbBr_3$ PNCs after the halogen exchange with Cl^-.

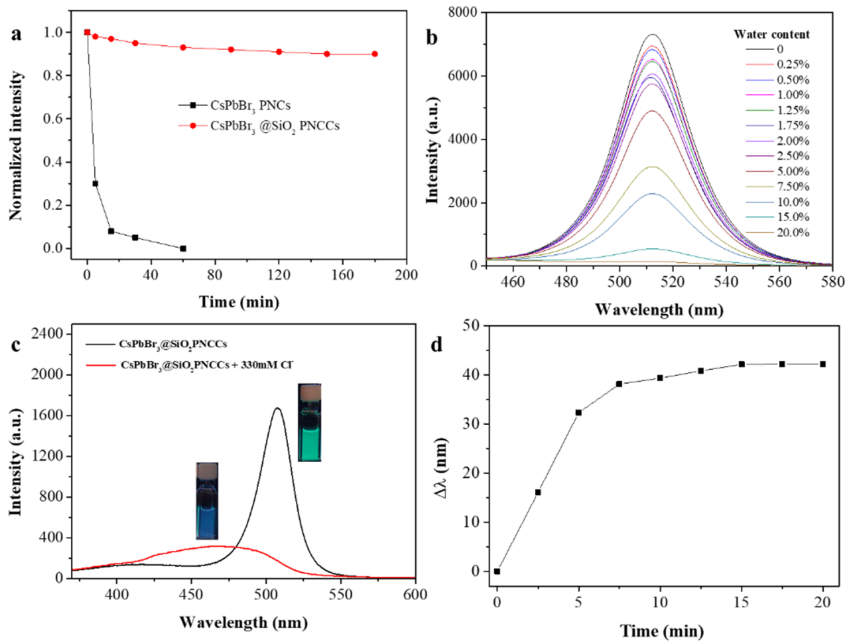


Figure 6. (**a**) Stability comparison between $CsPbBr_3$@SiO_2 PNCCs and $CsPbBr_3$ PNCs in ethanol; (**b**) $CsPbBr_3$@SiO_2 PNCCs in ethanol solution react with H_2O at different concentrations; (**c**) homogeneous halide exchanges between $CsPbBr_3$@SiO_2 PNCCs and Cl^- and their reaction optimization (**d**).

3.4. Analytical Performance of the Sensing Approach

For the investigation of the effects of the main co-existing substances in seawater, 1.92% (330 mmol/L) NaCl was selected as a typical test concentration due to its similar Cl^- concentration to seawater. The results shown in Figure S2 indicate that there is no obvious interference for the selected substances in the halogen exchange between $CsPbBr_3@SiO_2$ PNCCs and Cl^-, revealing good selectivity for the fluorescence sensing of Cl^- in seawater. Generally, another halogen ion, I^-, will notably affect the exchange with Cl^- at a similar concentration. Fortunately, the concentration of NaCl in the offshore seawater sample is about 1.92%, which is much higher than that of I^- (about 5 µmol/L) and results in negligible effects for I^-.

Under the selected sensing conditions, the fluorescence sensing of Cl^- based on the halogen exchange between $CsPbBr_3@SiO_2$ PNCCs and Cl^- was investigated. As shown in Figure 7, with the increase in Cl^- concentration, a blue shift of the fluorescence emission wavelength of $CsPbBr_3@SiO_2$ PNCCs can be clearly observed at an excitation wavelength of 365 nm. The observed color changes from greenish-blue-green to blue, which can be used for the rapid determination of Cl^- concentration in sea sand. In addition, the working curve of the system was plotted and showed a good relationship between the emission wavelength shift and the Cl^- concentration in the range of 0 to 3.0%, with a curve equation of $\Delta\lambda = 25.20\ C_{Cl^-} + 4.94$ and $R^2 = 0.9995$, and the limit of detection (LOD = 3σ/k, where σ is the relative standard deviation of 11 blank detection results, and k is the slope of the linear equation) is found to be 0.05 mg/g.

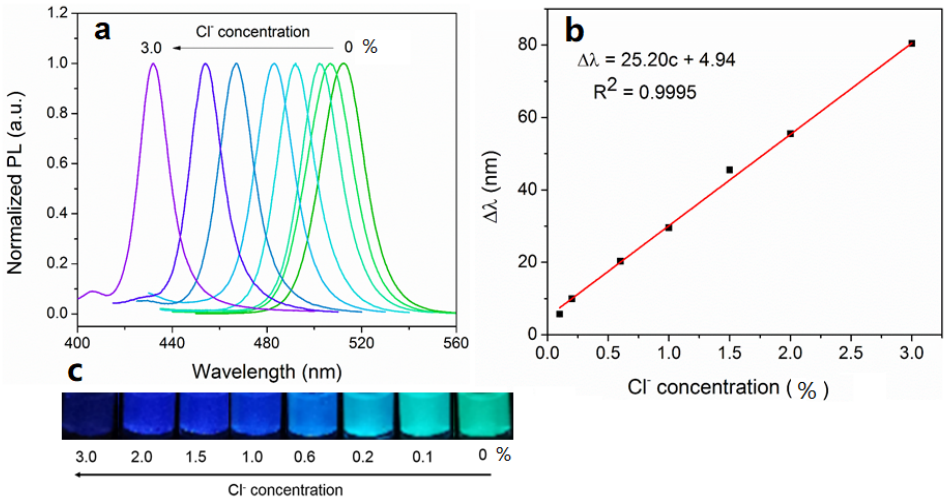


Figure 7. Fluorescence spectra and corresponding fluorescence photographs of the solutions in the presence of different concentrations of chloride from 0–3.0% at 365 nm UV excitation (**a**); working curve of the established fluorescent wavelength shift for the sensing of chloride in the range from 0 to 3.0% (**b**), as well as the corresponding colors for different concentrations of Cl^- (**c**).

In Figure 7c, it is easy to identify color changes for different concentrations of Cl^-. Typically, a green-blue to blue color was found when the Cl^- concentration was over 0.6 mg/g, which is the upper limit of Cl^- content for class III sand. As for higher-quality sand samples such as class I or II, the content of Cl^- should be less than 0.01% (0.1 mg/g) or 0.02% (0.2 mg/g), respectively. The observed color was bright green-blue and light blue, respectively, which makes the quality of the sand sample easy to identify with the naked eye using a color card.

In order to investigate the feasibility of the sensing approach, the NaCl concentration of seawater samples was firstly determined. The samples were directly processed in accordance with the experimental steps without any pre-treatment. As listed in the sensing results in Table S1, this method has a relatively good recovery in the range of 90% to 96.6%, indicating that the method is feasible for Cl^- sensing in seawater.

For the determination of the Cl^- concentration in sand samples, their filtrate was used to replace the Cl^- standard solution, and the semi-quantitative analysis of their concentration could be realized using a simple color card. As revealed in Table 1, the color difference between the three different sand samples could be easily observed. Obviously, the filtrate from the completely untreated sea sand produced the shortest emission wavelength (447 nm) and presented a blue color after 365 nm excitation. With the decrease in Cl^- concentration, which could be realized by freshwater cleaning, in sand samples II and III, the emission wavelength became red-shifted, and the observed color changed to dark blue-green (about 492 nm) and bright blue-green (506 nm). The quantitative analysis of the Cl^- concentration in the sand samples was carried out by using a fluorescence spectrophotometer. The accurate emission wavelength shifts were obtained and are listed in Table 1. The RSD and recovery results were found to be from 0.33% to 8.29% and 94% to 113%, respectively, indicating the applicability of the approach. In addition, the class discrimination for the sand samples became easy due to the obvious color differences between the different classes of sand. For example, the Sand 2 sample belongs to class III, and Sand 3 is class I.

Table 1. Determination of Cl^- in sand samples and their recoveries.

Sample	Emission Wavelength (nm)	Observed Color	Cl^- (%)	RSD (%)	Added Amount (%)	Emission Wavelength (nm)	Observed Color	Found (%)	Recovery (%)
Sand 1	447.0 ± 0.2		2.30	0.33	0.50	438.6 ± 0.1		2.7	94.07
Sand 2	492.6 ± 0.2		0.59	1.35	0.50	477.0 ± 0.2		1.2	110.44
Sand 3	506.0 ± 0.1		0.055	8.29	0.20	500.2 ± 0.2		0.29	112.85

4. Conclusions

In this study, $CsPbBr_3@SiO_2$ PNCCs were synthesized by a benzyl bromide nucleophilic substitution strategy in one step. The obtained $CsPbBr_3@SiO_2$ PNCCs reveal excellent luminescence performance and alcohol polarity stability. The homogeneous halogen exchange of NaCl solution (water)–$CsPbBr_3@SiO_2$ PNCCs (ethanol) can be achieved without pH regulation or magnetic stirring, which provides a very simple approach for Cl^- sensing in sand samples. The sensing color could easily be applied to identify the quality of sand samples, and of course, the quantitative analysis of Cl^- concentration could also be realized by their PL wavelength shift.

Supplementary Materials: The following supporting information can be downloaded at: https://www.mdpi.com/article/10.3390/chemosensors10050170/s1, Figure S1: Excitation spectrum of $CsPbBr_3@SiO_2$ PNCCs in the solution of 1.92% (330 mmol/L); Cl^-; Figure S2: The selectivity investigation on Cl^- determination in sea water based on $CsPbBr_3@SiO_2$ PNCCs halide exchanges with Cl^- (330 mmol/L). The potential coexistent ions in sea water from left to right were 20 µmol/L F^-, 0.7 mmol/L Br^-, 5 µmol/L I^-, 300 mmol/L Na^+, 10 mmol/L K^+, 20 mmol/L Mg^{2+}, 10 mmol/L Ca^{2+}, 50 µmol/L Sr^{2+}, 5 mmol/L CO_3^{2-}, 20 mmol/L SO_4^{2-}, 5 mmol/L HCO_3^-; Table S1: The determination of Cl^- in sea water. Excitation slit width, 1.5 nm; emission slit width, 5.5 nm, scan rate: 1200 nm·min^{-1}.

Author Contributions: Data curation, conceptualization and formal analysis, H.L. and F.L.; data curation, Y.H.; methodology and validation, Y.H. and L.Z.; visualization and writing—review and editing, M.Y., J.J.; project administration, supervision and writing of the original draft, X.C. All authors have read and agreed to the published version of the manuscript.

Funding: This research was funded by the National Natural Science Foundations of China, grant number 21876141.

Institutional Review Board Statement: Not applicable.

Informed Consent Statement: Not applicable.

Data Availability Statement: Data are contained within the article.

Conflicts of Interest: The authors declare no conflict of interest. The funders had no role in the design of the study; in the collection, analyses or interpretation of data; in the writing of the manuscript; or in the decision to publish the results.

References

1. *GB/T 14684-2011*; The General Administration of Quality Supervision, Inspection and Quarantine of the People's Republic of China. Sand for Construction. Standards Press of China: Beijing, China, 2011.
2. Calderón-Santiago, M.; Priego-Capote, F.; Jurado-Gámez, B.; Luque de Castro, M.D. Optimization study for metabolomics analysis of human sweat by liquid chromatography–tandem mass spectrometry in high resolution mode. *J. Chromatogr. A* **2014**, *1333*, 70–78. [CrossRef] [PubMed]
3. Doorn, J.; Storteboom, T.T.R.; Mulder, A.M.; de Jong, W.H.A.; Rottier, B.L.; Kema, I.P. Ion chromatography for the precise analysis of chloride and sodium in sweat for the diagnosis of cystic fibrosis. *Ann. Clin. Biochem.* **2014**, *52*, 421–427. [CrossRef] [PubMed]
4. Kubáň, P.; Greguš, M.; Pokojová, E.; Skřičková, J.; Foret, F. Double opposite end injection capillary electrophoresis with contactless conductometric detection for simultaneous determination of chloride, sodium and potassium in cystic fibrosis diagnosis. *J. Chromatogr. A* **2014**, *1358*, 293–298. [CrossRef]
5. Bujes-Garrido, J.; Izquierdo-Bote, D.; Heras, A.; Colina, A.; Arcos-Martínez, M.J. Determination of halides using Ag nanoparticles-modified disposable electrodes. A first approach to a wearable sensor for quantification of chloride ions. *Anal. Chim. Acta* **2018**, *1012*, 42–48.
6. Choi, D.-H.; Kim, J.S.; Cutting, G.R.; Searson, P.C. Wearable Potentiometric Chloride Sweat Sensor: The Critical Role of the Salt Bridge. *Anal. Chem.* **2016**, *88*, 12241–12247. [CrossRef] [PubMed]
7. De Matteis, V.; Cannavale, A.; Blasi, L.; Quarta, A.; Gigli, G. Chromogenic device for cystic fibrosis precocious diagnosis: A "point of care" tool for sweat test. *Sens. Actuators B Chem.* **2016**, *225*, 474–480. [CrossRef]
8. Chen, L.D.; Wang, W.J.; Wang, G.Z. Electrochemical Detection of Electrolytes Using a Solid-State Ion-Selective Electrode of Single-Piece Type Membrane. *Biosensors* **2021**, *11*, 109. [CrossRef] [PubMed]
9. Tsuchiya, K.; Akatsuka, T.; Abe, Y.; Komaba, S. Design of all-solid-state chloride and nitrate ion-selective electrodes using anion insertion materials of electrodeposited poly(allylamine)-MnO2 composite. *Electrochim. Acta* **2021**, *389*, 138749. [CrossRef]
10. Zhang, F.; Ma, C.; Jiao, Z.; Mu, S.; Zhang, Y.; Liu, X.; Zhang, H. A NIR Turn-on Fluorescent Sensor For Detection of Chloride Ions in vitro and in vivo. *Spectrochim. Acta A* **2020**, *228*, 117729. [CrossRef]
11. Tutol, J.N.; Lee, J.; Chi, H.; Faizuddin, F.N.; Abeyrathna, S.S.; Zhou, Q.; Morcos, F.; Meloni, G.; Dodani, S.C. A single point mutation converts a proton-pumping rhodopsin into a red-shifted, turn-on fluorescent sensor for chloride. *Chem. Sci.* **2021**, *12*, 5655–5663. [CrossRef]
12. Schazmann, B.; Alhashimy, N.; Diamond, D. Chloride Selective Calix[4]arene Optical Sensor Combining Urea Functionality with Pyrene Excimer Transduction. *J. Am. Chem. Soc.* **2006**, *128*, 8607–8614. [CrossRef]
13. Madhu, S.; Kalaiyarasi, R.; Basu, S.K.; Jadhav, S.; Ravikanth, M. A boron-dipyrrin–mercury(ii) complex as a fluorescence turn-on sensor for chloride and applications towards logic gates. *J. Mater. Chem. C* **2014**, *2*, 2534–2544. [CrossRef]
14. Bazany-Rodríguez, I.J.; Martínez-Otero, D.; Barroso-Flores, J.; Yatsimirsky, A.K.; Dorazco-González, A. Sensitive water-soluble fluorescent chemosensor for chloride based on a bisquinolinium pyridine-dicarboxamide compound. *Sens. Actuators B Chem.* **2015**, *221*, 1348–1355. [CrossRef]
15. Kim, J.P.; Xie, Z.; Creer, M.; Liu, Z.; Yang, J. Citrate-based fluorescent materials for low-cost chloride sensing in the diagnosis of cystic fibrosis. *Chem. Sci.* **2017**, *8*, 550–558. [CrossRef]
16. Riedinger, A.; Zhang, F.; Dommershausen, F.; Röcker, C.; Brandholt, S.; Nienhaus, G.U.; Koert, U.; Parak, W.J. Ratiometric Optical Sensing of Chloride Ions with Organic Fluorophore–Gold Nanoparticle Hybrids: A Systematic Study of Design Parameters and Surface Charge Effects. *Small* **2010**, *6*, 2590–2597. [CrossRef]
17. Ding, L.; Lian, Y.; Lin, Z.; Zhang, Z.; Wang, X.D. Long-Term Quantitatively Imaging Intracellular Chloride Concentration Using a Core-/Shell-Structured Nanosensor and Time-Domain Dual-Lifetime Referencing Method. *ACS Sens.* **2020**, *5*, 3971–3978. [CrossRef]
18. Xing, J.; Yan, F.; Zhao, Y.; Chen, S.; Yu, H.; Zhang, Q.; Zeng, R.; Demir, H.V.; Sun, X.; Huan, A.; et al. High-Efficiency Light-Emitting Diodes of Organometal Halide Perovskite Amorphous Nanoparticles. *ACS Nano* **2016**, *10*, 6623–6630. [CrossRef]
19. Sadhanala, A.; Ahmad, S.; Zhao, B.; Giesbrecht, N.; Pearce, P.M.; Deschler, F.; Hoye, R.L.Z.; Gödel, K.C.; Bein, T.; Docampo, P.; et al. Blue-Green Color Tunable Solution Processable Organolead Chloride–Bromide Mixed Halide Perovskites for Optoelectronic Applications. *Nano Lett.* **2015**, *15*, 6095–6101. [CrossRef]

20. Manser, J.S.; Christians, J.A.; Kamat, P.V. Intriguing Optoelectronic Properties of Metal Halide Perovskites. *Chem. Rev.* **2016**, *116*, 12956–13008. [CrossRef] [PubMed]
21. Liu, F.; Zhang, Y.; Ding, C.; Kobayashi, S.; Izuishi, T.; Nakazawa, N.; Toyoda, T.; Ohta, T.; Hayase, S.; Minemoto, T.; et al. Highly Luminescent Phase-Stable CsPbI3 Perovskite Quantum Dots Achieving Near 100% Absolute Photoluminescence Quantum Yield. *ACS Nano* **2017**, *11*, 10373–10383. [CrossRef]
22. Yan, F.; Xing, J.; Xing, G.; Quan, L.; Tan, S.T.; Zhao, J.; Su, R.; Zhang, L.; Chen, S.; Zhao, Y.; et al. Highly Efficient Visible Colloidal Lead-Halide Perovskite Nanocrystal Light-Emitting Diodes. *Nano Lett.* **2018**, *18*, 3157–3164. [CrossRef] [PubMed]
23. Bekenstein, Y.; Koscher, B.A.; Eaton, S.W.; Yang, P.; Alivisatos, A.P. Highly Luminescent Colloidal Nanoplates of Perovskite Cesium Lead Halide and Their Oriented Assemblies. *J. Am. Chem. Soc.* **2015**, *137*, 16008–16011. [CrossRef] [PubMed]
24. Yan, F.; Tan, S.T.; Li, X.; Demir, H.V. Light Generation in Lead Halide Perovskite Nanocrystals: LEDs, Color Converters, Lasers, and Other Applications. *Small* **2019**, *15*, 1902079. [CrossRef] [PubMed]
25. Protesescu, L.; Yakunin, S.; Bodnarchuk, M.I.; Krieg, F.; Caputo, R.; Hendon, C.H.; Yang, R.X.; Walsh, A.; Kovalenko, M.V. Nanocrystals of Cesium Lead Halide Perovskites (CsPbX3, X = Cl, Br, and I): Novel Optoelectronic Materials Showing Bright Emission with Wide Color Gamut. *Nano Lett.* **2015**, *15*, 3692–3696. [CrossRef]
26. Choi, Y.J.; Debbichi, L.; Lee, D.-K.; Park, N.-G.; Kim, H.; Kim, D. Light Emission Enhancement by Tuning the Structural Phase of APbBr3 (A = CH3NH3, Cs) Perovskites. *J. Phys. Chem. Lett.* **2019**, *10*, 2135–2142. [CrossRef]
27. Han, Y.; Sun, J.; Ye, S.; Zhang, Q. A stimuli responsive material of perovskite quantum dots composited nano-porous glass. *J. Mater. Chem. C* **2018**, *6*, 11184–11192. [CrossRef]
28. Sandeep, K.; Hamida, K.T. CsPbBr3 Perovskite–Coated Paper Substrate for the Cost-Effective Detection of Fluoride, Chloride, and Iodide Ions in Water. *Phys. Status Solidi A* **2021**, *218*, 2100101. [CrossRef]
29. Vasavi Dutt, V.G.; Akhil, S.; Mishra, N. Corrigendum: Cesium Lead Bromide Perovskite Nanocrystals as a Simple and Portable Spectrochemical Probe for Rapid Detection of Chlorides. *ChemistrySelect* **2021**, *6*, 12547. [CrossRef]
30. Li, F.; Feng, Y.; Huang, Y.; Yao, Q.; Huang, G.; Zhu, Y.; Chen, X. Colorimetric sensing of chloride in sweat based on fluorescence wavelength shift via halide exchange of CsPbBr3 perovskite nanocrystals. *Microchim. Acta* **2021**, *188*, 2. [CrossRef]
31. Wan, S.; Ou, M.; Zhong, Q.; Wang, X. Perovskite-type CsPbBr3 quantum dots/UiO-66(NH2) nanojunction as efficient visible-light-driven photocatalyst for CO2 reduction. *Chem. Eng. J.* **2019**, *358*, 1287–1295. [CrossRef]
32. Ou, M.; Tu, W.; Yin, S.; Xing, W.; Wu, S.; Wang, H.; Wan, S.; Zhong, Q.; Xu, R. Amino-Assisted Anchoring of CsPbBr3 Perovskite Quantum Dots on Porous g-C3N4 for Enhanced Photocatalytic CO2 Reduction. *Angew. Chem. Int. Ed.* **2018**, *57*, 13570–13574. [CrossRef]
33. Hu, Z.; Liu, Z.; Bian, Y.; Li, S.; Tang, X.; Du, J.; Zang, Z.; Zhou, M.; Hu, W.; Tian, Y.; et al. Enhanced Two-Photon-Pumped Emission from In Situ Synthesized Nonblinking CsPbBr3/SiO2 Nanocrystals with Excellent Stability. *Adv. Opt. Mater.* **2018**, *6*, 1700997. [CrossRef]
34. Li, X.; Wang, Y.; Sun, H.; Zeng, H. Amino-Mediated Anchoring Perovskite Quantum Dots for Stable and Low-Threshold Random Lasing. *Adv. Mater.* **2017**, *29*, 1701185. [CrossRef] [PubMed]
35. Zhao, W.; Hu, M.; Li, S.; Jiang, Y.; Zhang, X.; Hu, L.; Chen, H. The Solubility of Ternary System RbBr/CsBr-CH_3OH/C_2H_5OH-H_2O at Different Temperatures. *Acta Phys.-Chim. Sin.* **2007**, *23*, 695–700.